

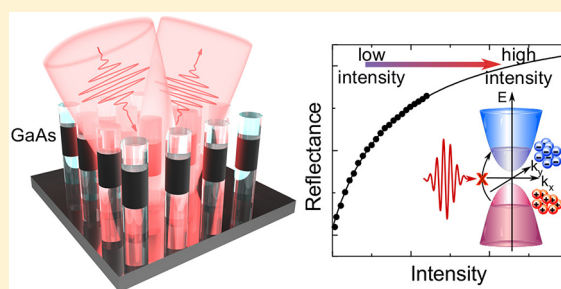
Low-Power Absorption Saturation in Semiconductor Metasurfaces

Varvara V. Zubyyuk,^{*,†,‡} Polina P. Vabishchevich,^{†,‡,§} Maxim R. Shcherbakov,^{†,||} Alexander S. Shorokhov,[†] Anna N. Fedotova,^{†,⊥} Sheng Liu,^{‡,§} Gordon Keeler,[‡] Tatyana V. Dolgova,[†] Isabelle Staude,[⊥] Igal Brener,^{‡,§} and Andrey A. Fedyanin^{*,†,||}[†]Faculty of Physics, Lomonosov Moscow State University, Moscow 119991, Russia[‡]Sandia National Laboratories, Albuquerque, New Mexico 87185, United States[§]Center for Integrated Nanotechnologies, Sandia National Laboratories, Albuquerque, New Mexico 87185, United States^{||}School of Applied and Engineering Physics, Cornell University, Ithaca, New York 14853, United States[⊥]Institute of Applied Physics, Abbe Center of Photonics, Friedrich Schiller University Jena, 07745 Jena, Germany

Supporting Information

ABSTRACT: Saturable optical elements lie at the cornerstone of many modern optical systems. Regularly patterned quasi-planar nanostructures—metasurfaces—are known to facilitate nonlinear optical processes. Such subwavelength semiconductor nanostructures can potentially serve as saturable components. Here we report on the intensity-dependent reflectance of femtosecond laser pulses from semiconductor metasurfaces with Mie-type modes, caused by the absorption saturation. Arrays of GaAs nanocylinders with magnetic dipole resonances in the spectral vicinity of the GaAs bandgap demonstrate a reduced saturation intensity and increased self-modulation efficiency, an order of magnitude higher than bulk GaAs or unstructured GaAs films. By contrast, the reflection modulation is shown to be negligible in the CW regime for the same average intensities, indicating that the process is not the result of temperature effects. Our work provides a novel idea for low-power saturable elements based on nonthermal nature of saturation. We conclude by devising a high-quality metasurface that can be used, in theory, to further reduce the saturation fluence below 50 nJ/cm².

KEYWORDS: absorption saturation, semiconductor metasurfaces, Mie-type resonance, I-scan



When a semiconductor is illuminated by photons with energies, $\hbar\omega$, exceeding its bandgap, E_g , an electron–hole plasma is generated. If $\hbar\omega \gtrsim E_g$, the states near the bandgap edge become rapidly occupied, preventing light from further absorption. This nonlinear optical phenomenon is widely known as saturable absorption (SA), the basis of many modern passively mode-locked and Q-switched lasers^{1–3} as well as of nonlinear filtering and optical signal processing solutions.^{4,5} Different devices and materials are used as saturable absorbers: direct-gap semiconductors, especially those of group III–V,^{6–8} thin layers of carbon nanotubes (CNT),^{9–11} graphene,^{12–14} semiconductor saturable absorber mirrors (SESAMs),^{3,15,16} and quantum dots.^{17–19} The saturation intensity of light I_s at which the extinction coefficient is reduced by a factor of 2 is an important parameter that determines the operation intensity of a saturable-absorber-based laser; in particular, low- I_s saturable optical components may lead to low-power, small-footprint femtosecond laser sources.

Nanostructured materials reduce the power requirements for many nonlinear optical processes. For example, ultrathin nanostructures either in the form of isolated nonlinear resonant nanoantennas^{20,21} or densely packed periodic arrays

of scatterers such as metasurfaces with tailored linear²² and nonlinear^{23–25} responses have been demonstrated for the enhanced second-harmonic^{26–30} and third-harmonic generation,^{31–33} nonlinear wavefront engineering,³⁴ optical switching^{35–37} and other nonlinearities, exceeding those of the constituent bulk materials. While plasmonic metasurfaces yield low nonlinear efficiencies, a more reassuring tendency was established with all-dielectric metasurfaces^{38–40} being practically lossless and thus capable of tolerating high-power fluence. Arrays of high-refractive-index dielectric nanoantennas also enable electromagnetically induced transparency⁴¹ or can be used as almost perfect reflectors due to extremely low absorption losses.⁴² GaAs was proposed as a constituent material for metasurfaces with Mie-type resonances⁴³ that improved second-harmonic generation^{44,45} and allowed for efficient all-optical tuning.⁴⁶ However, the benefits of Mie-type resonances for saturation effects have not been investigated yet.

In this letter, we experimentally demonstrate the self-modulation of femtosecond laser pulses due to the absorption saturation effect in semiconductor metasurfaces excited at their

Received: June 10, 2019

Published: October 4, 2019

fundamental Mie-type resonances. The intensity-dependent reflectance of femtosecond laser pulses with a photon energy of $\hbar\omega \approx 1.05E_g$ is observed in ordered arrays of subwavelength GaAs nanocylinders. The effect strongly depends on the diameter of the nanocylinders, reaching absolute reflectance modulation of up to 0.15 for a metasurface excited at the spectral vicinity of its magnetic dipole (MD) Mie-type resonance, as opposed to ~ 0.01 for bulk GaAs. We observe an increased self-modulation and a decrease in I_s for the resonant metasurfaces by more than 1 order of magnitude with respect to the unstructured GaAs film and bulk GaAs. Furthermore, we verify that thermal effects play a negligible role in the saturation mechanism by comparing the fs-pulse measurements to those obtained in the continuous wave (CW) regime under the same average laser power. The underlying principles of operating the metasurface as a saturable absorber are confirmed by rigorous full-wave simulations with a free-carrier density-dependent complex refractive index. We also numerically demonstrate that a high-quality metasurface provides a large modulation depth of up to 50% at low fluences down to 50 nJ/cm^2 . The studied metasurfaces may become a powerful tool for designing novel saturable elements in nanophotonic devices.

RESULTS

Concept and Samples. The main idea of the experiment is demonstrated in Figure 1. The metasurface with active elements in the form of GaAs nanocylinders is illuminated by a femtosecond pulse train; the reflected intensity is measured. As the intensity of the incoming pulses increases, the states in the conduction band (the upper energy states) get populated and the states in the valence band (the lower energy states) get depleted, thus eventually blocking any further light absorption, see regions (1), (2), and (3) in Figure 1. Optical properties of metasurfaces at the wavelength in the spectral vicinity of their intrinsic resonances are sensitive to the carrier concentration, since it affects the complex refractive index of the constituent material. The increase of carrier population manifests itself as a nonlinear increase in reflectance of the resonant metasurface with increasing illumination intensity, which we observe both experimentally and numerically.

The metasurfaces were fabricated using the recently published procedure^{43,44,46} that includes etching of GaAs/AlGaAs heterostructures through a SiO_x mask to create nanopillars, and subsequent wet oxidation of an AlGaAs layer to AlGaO with a low refractive index. The pillars were located on a bulk GaAs substrate that was used for reference measurements. Moreover, the results were compared with the measurements obtained by a three-layered ($\text{SiO}_x/\text{GaAs}/\text{AlGaO}$) part of an unstructured sample on a GaAs substrate (for more details see Supplementary Note S1).

The dimensions of the metasurfaces series were as follows: the diameters varied from $d = 140$ to 480 nm , the duty cycle (the ratio of the nanocylinder diameter to the array pitch) was 0.4 or 0.5, the height of the GaAs cylinders was $h = 300 \text{ nm}$, the AlGaO layer thickness was 330 nm , the SiO_x cap thickness was 200 nm . The scanning-electron microscopy images of typical structure of the metasurface are shown in the inset of Figure 2a. For the oblique-view image, the brighter areas in the center of the cylinders correspond to GaAs with a higher refractive index than that of the SiO_x and AlGaO layers.

Metasurfaces with the spectral position of Mie-type resonances close to the edge of the GaAs bandgap were

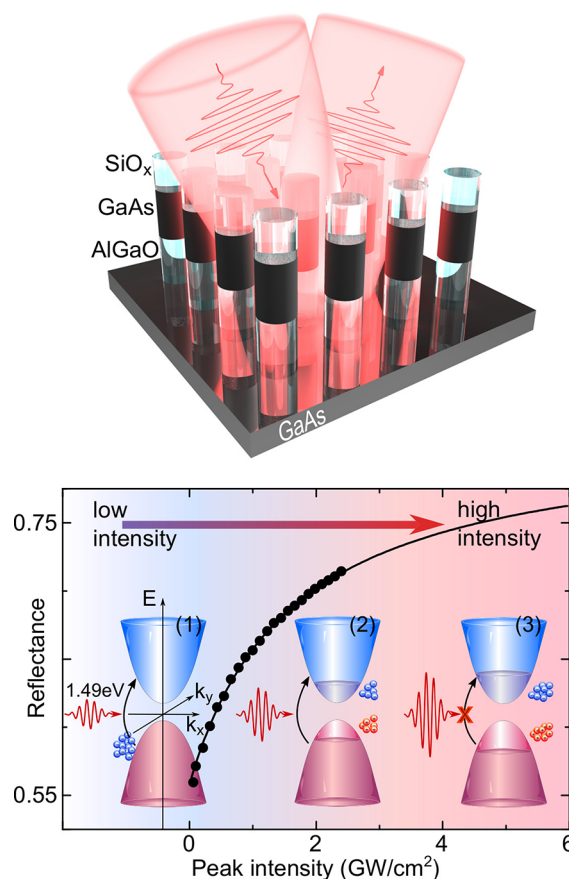


Figure 1. A self-modulation effect in resonant GaAs nanocylinders. Black curve and dots show the modulation mechanism of reflectance via the absorption saturation effect demonstrated by three regions: (1) low intensity with linear absorption, the middle region (2) when the generated carriers change the parameters of the medium thus modifying the reflectance, and (3) with high intensity when the medium can no longer absorb the input illumination due to Pauli blocking.

chosen in order to efficiently utilize the interband transitions and saturate the absorption in GaAs (at room temperature the energy gap $E_g = 1.42 \text{ eV}$ or about 870 nm). Figure 2a shows the measured reflectance spectra of a metasurface sample with $d = 195 \text{ nm}$, exhibiting a resonant behavior of the metasurface for s -polarized light at different angles of incidence. To identify the nature of the observed resonances, numerical simulations using the finite-difference time-domain (FDTD) method were performed. In Figure 2b the reflectance spectrum of the metasurface shows a peak corresponding to the MD mode of the GaAs nanocylinders. The analysis of the local field maps within the GaAs nanocylinder reveals the presence of an ED resonance in the vicinity of the MD resonance; however, the amplitude of the former is much smaller than that of the latter. The local electric field distribution at a wavelength of 875 nm presented in the inset of Figure 2b displays a characteristic MD resonance profile in high-index nanoparticles.^{47,48} The reflectance spectra did not exhibit apprehensible sensitivity to the polarization of light at normal incidence. The experimental angular dependences in Figure 2a and corresponding simulations (for angles up to 60 degrees please refer to Supplementary Figure S2e) show that the spectral position of the MD mode does not significantly depend on the angle of incidence for s -polarized light in the studied range of angles.

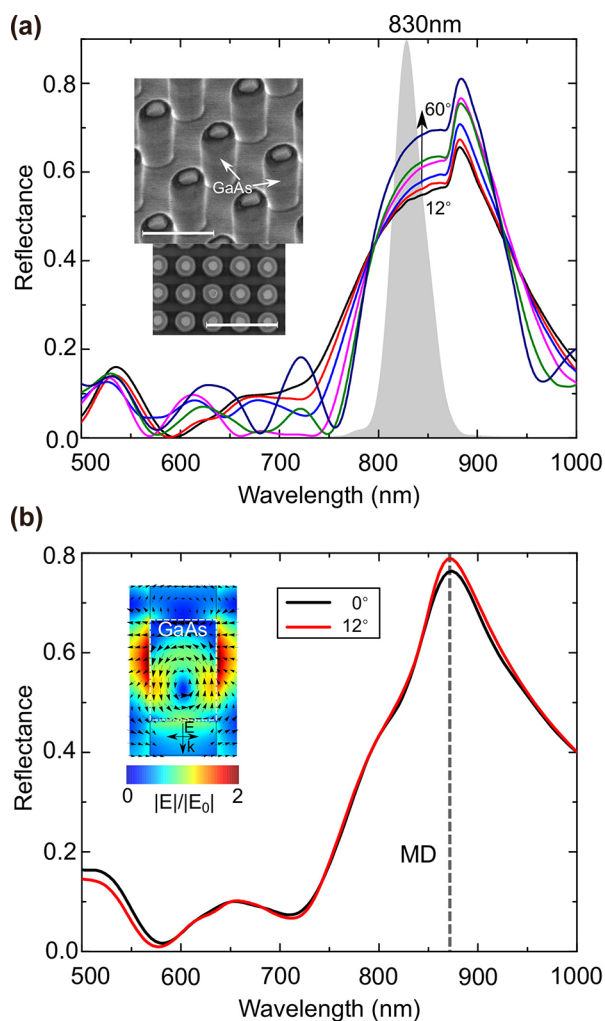


Figure 2. Reflectance spectra of the metasurface for *s*-polarized incident light. (a) Experimental angular dependence of the reflectance spectrum from 12° (red curve) to 60° (navy blue curve) incidence angle and a typical excitation laser spectrum used in the experiments (gray area). Inset: a scanning-electron micrograph of the samples: the top-view for the samples with $d = 195$ nm and the oblique-view for the $d = 400$ nm fabricated on the same chip. In the oblique-view image, the brighter areas in the center of the cylinders correspond to the GaAs layer. Scale bars are $1 \mu\text{m}$. (b) A simulated reflectance spectrum at 0° (black curve) and 12° (red curve) incidence angle for the metasurface with the following parameters: the period of the structure is 385 nm, and the diameter is 196 nm. Inset: the local electric field map at 875 nm. The GaAs bandgap is at 1.42 eV (~ 870 nm).

However, this is not the case for *p*-polarized light (Supplementary Figure S2), which indicates a certain degree of coupling between the nanocylinders.⁴⁹ The experimental data are in good overall agreement with the numerical simulations. All experimental spectra of the metasurfaces have a feature at $\lambda = 880$ nm that is attributed to the peculiarity of GaAs refractive index dispersion near its bandgap,^{50,51} which was not taken into account in the simulations. The samples with smaller diameters were also studied and shown to have the MD mode at the wavelengths shorter than the absorption edge of GaAs. As demonstrated below, the resonances have low-quality factors due to the interband absorption in GaAs.

Experimental Demonstration of Saturation in GaAs Metasurfaces. We performed the open aperture intensity

scan (*I*-scan) measurements in order to demonstrate reflectance tuning in metasurfaces.^{52,53} The setup is schematically shown in Figure 3a. Femtosecond pulses from a Ti:sapphire laser with a repetition rate of 80 MHz were focused into a spot $\approx 20 \mu\text{m}$ in diameter. *I*-scan experiments were performed at $\lambda_0 \approx 830$ nm with a pulse spectral full width at half-maximum of 40 nm, a pulse duration of 60 fs, and *s*-polarized light. We chose the laser wavelength $\lambda_0 \approx 830$ nm as a pump since $\hbar\omega_0 > E_g$ so that the linear absorption is still significant for the pump wavelength. At the same time, the Mie-type resonances of the metasurfaces were efficiently excited in this wavelength range. Significant variations in the optical response of the metasurfaces due to the sensitivity of the Mie-type resonance to the complex refractive index of the semiconductor that changes under photoinjection of electron–hole pairs are expected.

Here we concentrate on the metasurface with $d \approx 195$ nm exhibiting the MD resonance at $\lambda_{\text{MD}} \approx 880$ nm. The reflectance was measured as a function of the peak intensity. Figure 3b,c shows nonlinear behavior and a considerable increase in the reflectance of the metasurface (black dots) with increasing incident peak intensity. Compared to the bulk GaAs substrate (blue dots in Figure 3b), the reflectance change is enhanced by more than an order of magnitude for the metasurface. Solid curves of the corresponding colors are the numerical fits to the phenomenological model discussed below. The red dashed line denotes the I_s parameter—a characteristic intensity at which the nonlinear addition to reflectance is half its maximum value. The shaded area at high intensities in Figure 3b corresponds to the estimated intensity range above the irreversible damage threshold for the metasurface (see Methods for detailed information).

We performed *I*-scan measurements for the metasurfaces under CW illumination for the same central wavelength and the same range of average intensities in order to demonstrate that the increase in the reflectance cannot be caused by temperature change and primarily results for the free-carrier generation (red dots in Figure 3c). The *I*-scan measurements were carried out at a small angle of incidence θ (detector position 2 in Figure 3a) to increase the amount of signal. The intensity dependence of the reflectance coefficient in the CW mode shows a constant behavior with a small decrease, which we attribute to the instability of the laser in the CW regime and reflectivity changes due to sample heating. The schematic images of the bandgap in two cases are shown in the inset of Figure 3c. The linear regime demonstrates absorption under CW illumination and under low-power femtosecond (FS) pulses and shows the possibility absorption in the linear regime. The nonlinear regime obtained for high-power FS pulses illustrates the population of the states close to the bandgap due to injected free-carriers which leads to pronounced reflectance changes.

Figure 4a shows the data on the reflectance tuning for four metasurfaces with cylinders of various diameters ranging from largest (i) to smallest (iv). An *I*-scan trace for the substrate (s) is also shown. Significant reflectance changes are only observed for the resonant metasurface. The respective experimental reflectance spectra at normal incidence are displayed in Figure 4b by solid curves; the dotted curves correspond to numerically simulated spectra. In the case of the smallest cylinder diameter (iv) the Mie-type resonances are located in a shorter-wave range, but, due to the absorption of GaAs, it has a

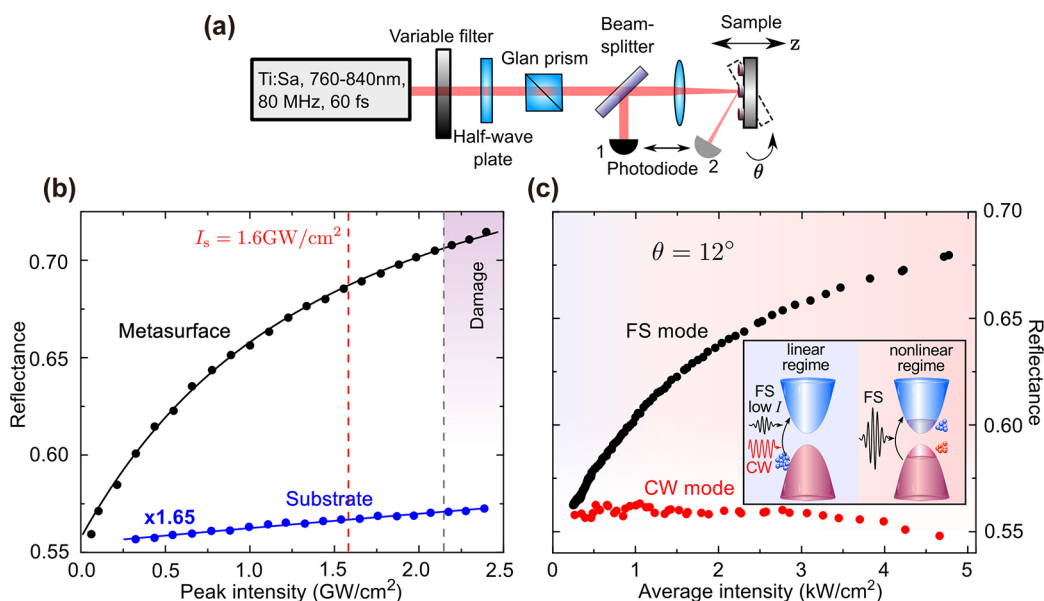


Figure 3. Experimental self-modulation reflectance tuning of the GaAs metasurface. (a) Setup for I -scan measurements: the reflectance is measured as a function of incident power. (b) Experimentally measured power-dependent reflectance for the metasurface (black dots) and for the substrate (blue dots; values are multiplied by 1.65 for better visibility) under femtosecond (FS) illumination at normal incidence. The metasurface has the following parameters: the period of the structure is 385 nm and the diameter of the cylinders is 196 nm. Solid curves of the corresponding colors are numerical fits to eq 1; the red dashed line corresponds to the saturation intensity I_s . The shaded area indicates the range of the irreversible damage. (c) Intensity-dependent reflectance for the metasurface under FS (black dots) and continuous wave (CW) (red dots) illumination at $\theta = 12^\circ$. The inset illustrates the GaAs bandgap in the following cases. The left panel stands for both CW and low-intensity FS modes, where the band-edge states are unsaturated and the regime is linear. The right panel stands for the population of the band-edge states at a higher intensity in the FS mode; here, the states are saturated and the regime is nonlinear.

low-quality factor and becomes almost nonresonant, as in the case of the substrate (purple curve).

Saturation Model. The I -scan traces exhibit a typical saturable behavior. Before discussing the microscopic origins of saturation in metasurfaces, we construct a phenomenological model for experimental curves that saturate as a function of intensity I :

$$R(I) = R_1 - \frac{\Delta R}{1 + I/I_s} \quad (1)$$

where $\Delta R = R_1 - R_0$ is the reflectance modulation, R_1 is the reflectance at high intensities ($I \gg I_s$), R_0 is the linear reflectance for close-to-zero intensity, I is the input intensity, and $R(I)$ is the intensity-dependent reflectance. Such dependence provides an excellent description of the experimental data, as shown in Figure 3b and Figure 4a by solid curves and dots (model and experimental results, respectively). The curves were obtained by fitting this model to experimental data and the I_s parameter for each of the resonant samples was determined. The I_s parameter characterizes how sensitive the metasurface is to the incident illumination: the smaller the I_s parameter, the less energy is needed to saturate the system and to change the reflectance significantly. The slope dR/dI at about $I \approx 0$ can also be used to characterize the nonlinear behavior and the efficiency of the reflection modulation. Below, we compare I_s and $dR/dI|_{I \approx 0}$ that were experimentally measured.

The values obtained from the fit for the resonant case are $I_s = 1.1 \text{ GW/cm}^2$ for sample (i), 1.3 GW/cm^2 for sample (ii), and 1.6 GW/cm^2 for sample (iii), as shown in Figure 4a. In the cases of nonresonant sample (iv) and substrate (s) in Figure 4, the measured data corresponds to the beginning of the

saturation curve, thus the I_s value is beyond the experimental range and cannot be unambiguously determined from the fit. We can conclude that the Mie-type resonances for three metasurfaces with larger diameters have appropriate spectral positions with respect to the laser wavelength used. Comparing $dR/dI|_{I \approx 0}$ also indicates that these metasurfaces are an order of magnitude more sensitive to the incident illumination than the nonresonance metasurface and bulk GaAs (see Figure 4a).

We see two possible explanations to the enhanced saturation observed in resonant metasurfaces. First, the local electromagnetic field is enhanced at Mie-type resonances, providing higher free carrier (FC) generation rates for the same intensity, if compared to the bulk semiconductor. Second, the reflectance spectrum is sensitive to the FC concentration, and, therefore, to the incident power. Judging from the local field distribution in Figure 2b, the overall intensity enhancement within the nanocylinders is quite subtle, by a factor of <1.5 , which cannot make up for the observed saturation. Therefore, here, we attempt to reconstruct the saturable behavior of the metasurfaces by modeling the FC response of the semiconductor.

Principle of Charge-Induced Changes in GaAs Metasurfaces. The observed modulation of the reflection is caused by three mechanisms of refractive index modulation in GaAs:⁵⁴

$$\begin{aligned} \Delta n &= \Delta n_{\text{DT}} + \Delta n_{\text{BF}} + \Delta n_{\text{BS}} \\ \Delta \kappa &= \Delta \kappa_{\text{BF}} + \Delta \kappa_{\text{BS}} + \Delta \kappa_{\text{DT}} < 0 \end{aligned} \quad (2)$$

where Δn and $\Delta \kappa$ are changes in the real and imaginary parts of the GaAs refractive index, respectively, and the indices DT, BF, and BS denote the three terms: Drude term, bandfilling, and bandgap shrinkage (renormalization). These terms can

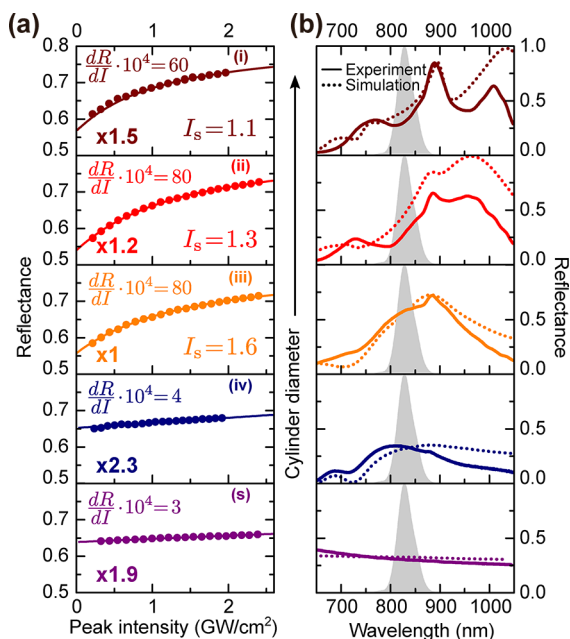


Figure 4. (a) Experimental I -scan traces (dots) and their best numerical fits (curves) for different metasurfaces (i)–(iv) with diameters of 250, 238, 196, and 140 nm, respectively, and the GaAs substrate (s). Note that the multiplication coefficients are introduced for clarity, and fitting was performed before they were applied to the data. The I_s parameter, measured in GW/cm^2 , and the slope $dR/dI|_{I \rightarrow 0}$ are the values obtained from the fitting procedure. (b) Corresponding reflectance spectra and the femtosecond pulse spectrum (gray shaded areas). The three upper graphs refer to the samples (i)–(iii) with the spectral position of Mie-type resonances in the vicinity of the laser illumination. The solid and the dotted curves correspond to the experimental and numerically simulated spectra, respectively.

lead to both positive and negative contributions to the real part of the refractive index n and to negative contributions to the extinction coefficient κ . We carried out FDTD simulations of the reflectance spectra in order to demonstrate that metasurfaces with Mie-type resonances in GaAs nanocylinders are much more sensitive to low-power laser stimulation than nonresonant structures or bulk materials and can reveal nonlinear behavior as saturable optical absorbers caused by injected FCs. Reflectance spectra of the metasurface are calculated with the dielectric function of GaAs modified by the corresponding changes in the refractive index for different incident power values according to eqs 2 (see Methods for detailed information). Simulated reflectance at 830 nm is plotted in Figure 5a as a function of the incident beam power along with the corresponding changes in the refractive index in the inset. The nonmonotonic behavior of Δn and $\Delta \kappa$ as functions of incident power is demonstrated in Figure 5b by dashed and solid curves, respectively. There are both negative and positive values of $\Delta n(I)$ leading to the blue and to the red shifts of the resonance, respectively. The advantage of operating with photon energy larger than the bandgap is the presence of absorption, which allows to obtain significant changes in the imaginary part of the refractive index in addition to the changes in the real part due to FC injection. The dominant contributions to the change in the extinction coefficient are BS and BF, the contribution of DT is more than 20 times smaller compared to BF and it will not be taken into account. We performed full-wave numerical simulations of the metasurface response for four cases to show how the

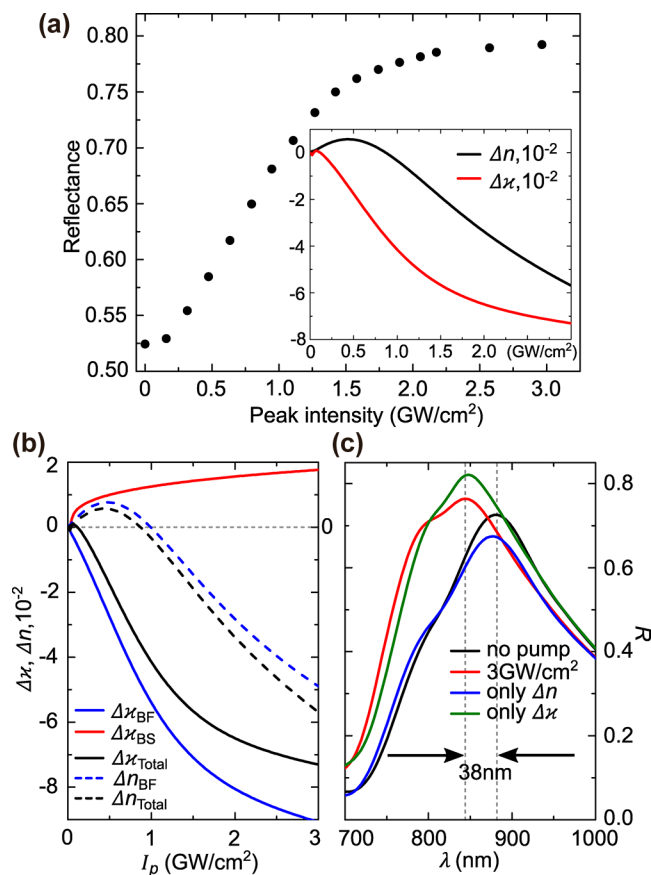


Figure 5. Simulations. (a) Reflectance as a function of the incident beam power for the metasurface (iii) with period of the structure of 385 nm and cylinder diameter of 195 nm. Inset: Changes in refractive index and extinction coefficient. (b) Dominant effects: bandfilling (BF) and bandgap shrinkage (BS) and the total contribution to changes in real and imaginary parts of refractive index as a function of the incident beam power. (c) Unperturbed reflectance spectrum (black curve), the reflectance spectrum with changed $\Delta \kappa$ and Δn under free-carriers generation induced at $\sim 3 \text{ GW}/\text{cm}^2$ (red curve), the reflectance spectra with changes only in Δn or $\Delta \kappa$ in blue and green curves, respectively.

resonance is modified under FC generation. The first case is the equilibrium state of the metasurface with the complex dielectric permittivity function of GaAs from Palik dispersion data,⁵⁵ as shown in Figure 5c and Figure 2b by a black curve. The second one (red curve in Figure 5c) is the same data of the complex dielectric permittivity of GaAs but with the added changes in refractive index and extinction coefficient determined by FCs induced at 3 GW/cm^2 of input intensity (estimated plasma density of $N \approx 5 \times 10^{18} \text{ cm}^{-3}$). The other cases include the changes added either in refractive index or in extinction coefficient in blue and green curves, respectively. Figure 5c demonstrates that in our case the reflectance increases mostly due to the decrease in absorption. We also verified that changes in complex dielectric permittivity in the GaAs substrate did not affect the reflectance spectrum of the metasurface under pump illumination. It can be concluded therefore that the metasurfaces under study show saturation of reflectance due to saturation of absorption in its GaAs nanocylinders.

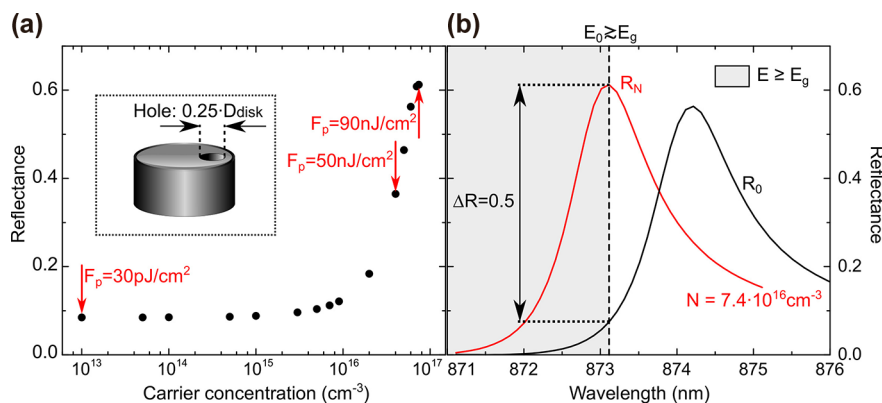


Figure 6. Simulations. (a) Reflectance as a function of the induced free-carriers concentration for the high-Q metasurface in a logarithmic scale. Inset: An array unit of the high-Q metasurface (see [Methods](#) for the exact dimensions). Red arrows indicate several estimated corresponding pump fluences. (b) Unperturbed reflectance spectrum R_0 (black curve) and the reflectance spectrum R_N (red curve) with changed Δn and $\Delta\alpha$ according to a free-carrier concentration of $N = 7.4 \times 10^{16} \text{ cm}^{-3}$ at the energy E_0 in the vicinity of the bandgap edge E_g .

DISCUSSION

Resonant metasurfaces reveal strong nonlinear behavior of reflectance and low I_s values. Furthermore, comparing to previous findings, the operating fluences of GaAs metasurfaces are much lower than those needed in metallic^{56,57} or silicon-based^{36,58} metasurfaces; for example, in sample (iii) the observed relative reflectance change is 0.3 at a fluence of $140 \mu\text{J}/\text{cm}^2$ ($2.3 \text{ GW}/\text{cm}^2$). However, the quality factors (Q) of the metasurfaces under study were kept at very modest values; below, we show that the use of high- Q resonances can lead to an even more drastic reduction of I_s .

Breaking a certain symmetry in the plane of metallic and dielectric structures can lead to resonances with very high Q -factors.^{59–62} We chose the nanodisk with a hole shifted from the disk center along the diameter as an elementary unit of our high- Q metasurface with a Q -factor about 500, as shown in the inset of [Figure 6a](#) (see [Methods](#) for the exact dimensions). Such a system is mirror-symmetric, where the input linear polarization is unchanged upon reflection, which is essential for laser applications. Simulated reflectance at the energy $E_0 \gtrsim E_g$ is plotted in [Figure 6a](#) as a function of the induced free-carriers concentration in a logarithmic scale. The value of E_0 was chosen very close to the bandgap edge, to attain absorption small enough to exhibit the high- Q resonance, but not zero, to obtain the contribution from absorption change. Under nonperturbative intensities, the absorption coefficient is $\alpha_0 = 129 \text{ cm}^{-1}$, and the refractive index is $n_0 = 3.5932$. In [Figure 6a](#), the reflectance dependence demonstrates a typical behavior of a saturable absorber. The saturation effect is present only for one of the linear polarizations (see [Methods](#) for the detailed information). The characteristic pump fluences needed to inject the corresponding amount of free-carriers are marked by red arrows and show that one needs only $50 \text{ nJ}/\text{cm}^2$ to achieve more than 50% of modulation depth with respect to R_0 . Under a free-carrier density $N = 7.4 \times 10^{16} \text{ cm}^{-3}$ at the energy E_0 , the refractive index and absorption coefficient are reduced by $\Delta n = -5.7 \times 10^{-3}$ and $\Delta\alpha = 21$. This leads to the shift and increase of R_0 up to R_N , as shown in [Figure 6b](#) by black and red curves, respectively (see [Methods](#) for detailed information). There is a certain roll-off in reflectance at higher fluences $F_p > 90 \text{ nJ}/\text{cm}^2$ associated with the bandgap shrinkage effect, which leads to $\Delta\alpha > 0$, and we also expect a fairly low damage threshold. This puts some limitation on the operating power range and thus restricts, for example, the laser pulse energy and its stability in

real applications. However, we find this design especially attractive for a laser system that requires ultralow power operation. A comparison of GaAs metasurface saturable absorbers with other types of saturable absorbers—including SESAMs, carbon nanotubes, nanoparticles, and graphene—is included in the [Supplementary Note S3](#).

In summary, we have designed and fabricated nonlinear metasurfaces that show pronounced reflectance saturation owing to absorption saturation in Mie-resonant GaAs nanoparticles resonances. The observed self-modulation of femtosecond laser pulses in resonantly excited metasurfaces was typically an order of magnitude higher than in bulk GaAs or in an unstructured GaAs film. The comparison of self-modulation in the femtosecond regime and the CW regime under the same average intensities obviously indicates the nonthermal nature of self-modulation. We attribute the reflectance increase to free-carrier-induced changes mainly in the imaginary part of the refractive index, as revealed by full-wave numerical simulations. The main achievement of the presented work is in the demonstration of decreased I_s parameter and increased self-modulation efficiency for the resonant semiconductor metasurfaces. We expect a picosecond time scale operation of such reflectance modulation device.⁴⁶ Additional numerical simulations show that symmetry-broken metasurfaces allow to achieve a saturable absorber with significantly improved characteristics, such as very low saturation fluence and high modulation depth. These metasurfaces can serve as ultra-compact saturable absorbers and can become backbones for novel photonics devices, for example, low-threshold pulsed laser sources or optical noise filters.

METHODS

Nonlinear-Optical Measurements. We used femtosecond laser pulses from a Ti:sapphire laser (Coherent Micra 5) with an average output power of 250 mW and a repetition rate of 80 MHz for I -scan measurements. The laser illumination passed through a variable density filter to control the incident power on the sample in the range from 0.01 to 40 mW, a broadband half-wave plate to set the polarization (spectral range 600–1100 nm) and a Glan–Taylor prism. The mutual position of the plate and prism can also be used to control the incident power. In the experiment, reflectance was measured instead of transmittance because of the thick and opaque GaAs substrate. A nonpolarizing beamsplitter and a

photodiode were used in position 1 as shown in Figure 3 in order to be able to measure under normal incidence. Position 2 of the photodiode was used for angular-dependent reflectance. The *I*-scan measurements for CW illumination were also carried out under non-normal incidence angle $\theta = 12^\circ$ to increase the amount of signal that is otherwise lost on multiple reflections from the beamsplitter. The laser pulses were focused at the sample onto a spot with a diameter of $\approx 20 \mu\text{m}$ by a lens with a focal length of $f = 45 \text{ mm}$. The sample was placed on a three-coordinate translation stage. The setup also allowed to use it for *z*-scan experiments by moving the sample along the optical axis of the focusing system (for more details see Supplementary Note S1). The wavelength of the pulse train is at wavelengths that were close enough to the bandgap of GaAs to generate a large number of free carriers and benefit from the Mie-type resonance of the sample. We obtained values for the damage threshold by gradually increasing the fluence and decreasing it back to the initial value. If, after a certain fluence, the reflectance of the metasurface decreased in comparison to the initial one, and did not recover minutes after the laser beam was blocked, then this fluence value was taken as the damage threshold.

Calculations of Charge-Induced Complex Refractive Index. We estimated the carrier-induced changes in refractive index for GaAs by taking into account three carrier effects: bandfilling, bandgap shrinkage, and the Drude term. The bandfilling-induced change in absorption for photon energies of $E \geq E_g$ under the parabolic band assumption⁵⁴ is

$$\Delta\alpha_{\text{BF}}(E, N_{e,h}) = \frac{C}{E} \sqrt{E - E_g} [f_v(E_a) - f_c(E_b) - 1] \quad (3)$$

where N_e, N_h are the densities of free electrons and holes, respectively (we assume $N_e = N_h$ and thus omit the index in $N_{e,h}$ subsequently), C is a constant, $f_v(E_a)$ is the probability of a valence band state of energy E_a , occupied by an electron, and $f_c(E_b)$ is the probability of a conduction band state of energy E_b , occupied by an electron and described by the Fermi–Dirac distribution.

The bandgap shrinkage-induced change in absorption is

$$\Delta\alpha_{\text{BS}}(E, N) = \frac{C}{E} \sqrt{E - E_g - \Delta E_g(N)} + \frac{C}{E} \sqrt{E - E_g} \quad (4)$$

where N is the concentration of free electrons or holes and

$$\Delta E_g(N) = \frac{\kappa}{\epsilon_s} \left(1 - \frac{N}{N_{\text{cr}}}\right)^{1/3} \quad N \geq N_{\text{cr}}$$

$$\Delta E_g(N) = 0 \quad N < N_{\text{cr}} \quad (5)$$

where $\kappa = 0.13$ is an adjustable parameter, $\epsilon_s = 13.1$ is the relative static dielectric constant of GaAs, and $N_{\text{cr}} = 7.4 \times 10^{16} \text{ cm}^{-3}$ is the critical concentration of free carriers.

The real and imaginary parts of the refractive index $\hat{n} = n + i\kappa$ are dependent and linked by the Kramers–Kronig relations. Thus, any change in the absorption coefficient $\Delta\alpha$ is accompanied by a change in the real refractive index Δn . It means that the induced change in the real refractive index can be expressed through the change in the absorption coefficient in the following form:

$$\Delta n_{\text{BF,BS}}(N, E) = \frac{2c\hbar}{e^2} \text{PV} \int_0^\infty \frac{\Delta\alpha_{\text{BF,BS}}(E', N)}{E'^2 - E^2} dE' \quad (6)$$

where $\Delta\alpha_{\text{BF,BS}}(E, N)$ is the absorption modification from eqs 3 and 4 for photon energies E , and “PV” denotes the principal value.

Changes in the real refractive index due to the intraband free-carrier absorption can be written via the Drude model as follows:

$$\Delta n_{\text{D}}(N, E) = -\left(\frac{e^2 \lambda^2}{8\pi^2 c^2 \epsilon_0 n}\right) \left\{ \frac{N_e}{m_e} + N_h \frac{m_{\text{hh}}^{1/2} + m_{\text{lh}}^{1/2}}{m_{\text{hh}}^{3/2} + m_{\text{lh}}^{3/2}} \right\} \quad (7)$$

where m_e, m_{lh} , and m_{hh} are the effective masses of electrons, light holes, and heavy holes, respectively, n_0 is the index of GaAs, and ϵ_0 is the permittivity of vacuum. We estimate the density of injected FCs as $N = EA_0/(E_{\text{pump}}VN_d)$, where E is the pulse energy, A_0 is the small signal absorptance, $E_{\text{pump}} = E_0 = 1.42001 \text{ eV}$, V is the GaAs cylinder volume, and N_d is the number of GaAs cylinders.

Numerical Simulations. We used the commercial software package Lumerical FDTD solutions for the numerical simulation of the nonlinear reflectance behavior of GaAs metasurface; we applied periodic boundary conditions and plane wave excitation from the top. The dimensions of the structure were as following: the period of the structure was 635, 480, 385, and 280 nm for (i)–(iv) metasurfaces, respectively; the SiO_x cap was 200 nm in height, the GaAs nanocylinder was 300 nm in height, the AlGaO layer is 330 nm in height, and the diameter of the whole pillar was taken to be 250, 238, 196, and 140 nm for (i)–(iv) metasurfaces, respectively. The discrepancy between the diameter taken from the scanning-electron microscopy images and the one used in simulations may be due to the deviations of the fabricated pillars from a perfect cylindrical shape. For these simulations, we took dispersionless refractive indices of 1.6 and 1.45 for AlGaO⁴³ and SiO_x , respectively. For the complex dielectric permittivity function of GaAs we use experimental data from Palik,⁵⁵ to which we added the changes caused by induced dense e–h plasma. The AlGaO oxide pedestal and the cap layer were modeled as nondispersive dielectric media with $n = 1.6$ and $n = 1.45$, respectively.

The metasurfaces with high-Q resonances we modeled as an array of single GaAs nanodisks with holes with the following parameters: the period of the structure was 671.5 nm, nanodisk height was 117 nm, the diameter was 256 and 64 nm for the disk and hole, respectively; the shift distance of the hole regarding the disk center along the diameter was 57 nm. The refractive index and the extinction coefficient for the unperturbed spectrum R_0 were chosen as a constant $n_0 = 3.5932$ and $\kappa_0 = 8.95 \times 10^{-4}$ ($\alpha_0 = 129 \text{ cm}^{-1}$), respectively. These values are for $E_0 = 1.42001 \text{ eV}$ energy used for calculations of charge-induced changes in the complex refractive index. The resonance for such metasurface has a Q-factor of approximately 500. The high-Q mode is excited when the polarization of the input light directed along the asymmetry axis. The numerical simulations of the reflectance spectra were performed in the spectral range around the E_0 , but only this point was used to determine the magnitude of the reflectance coefficient. Taking the material dispersion into account slightly modifies the spectrum in the neighborhood of that energy point in contrast to a dispersionless structure with n_0 and κ_0 . The polarization of the electric field was directed along the asymmetry axis. The presence of the substrate and the AlGaO nanodisk slightly modify the properties of the

resonance such as central wavelength, modulation depth, and the quality factor. The room temperature $T = 300$ K was used throughout the simulations.

■ ASSOCIATED CONTENT

■ Supporting Information

The Supporting Information is available free of charge on the ACS Publications website at DOI: 10.1021/acsp Photonics.9b00842.

z-scan measurements, experimental reflectance spectroscopy details, and related simulation results (PDF)

■ AUTHOR INFORMATION

Corresponding Authors

*E-mail: zubyuk@nanolab.phys.msu.ru.

*E-mail: fedyanin@nanolab.phys.msu.ru.

ORCID

Varvara V. Zubyuk: 0000-0003-2337-4905

Polina P. Vabishchevich: 0000-0003-0795-2314

Sheng Liu: 0000-0001-5644-7715

Isabelle Staude: 0000-0001-8021-572X

Igal Brener: 0000-0002-2139-5182

Andrey A. Fedyanin: 0000-0003-4708-6895

Notes

The authors declare no competing financial interest.

■ ACKNOWLEDGMENTS

The authors acknowledge fruitful discussions with B. Luk'yanchuk and A. Evlyukhin. The authors thank G. Peake for samples fabrication and D. Yagudin for numerical simulations of the mode decomposition. Financial support from Ministry of Science and Higher Education of Russian Federation (grant N 14.W03.31.0008 (I-scan), RFBR grant N 18-29-20097 (optical spectra measurements), Russian Science Foundation (grant N 18-12-00475, analytical calculations), and by the German Research Foundation through the Emmy Noether Programme (STA 1426/2-1) is gratefully acknowledged. The research is supported by MSU Quantum Technology Center. Parts of this work were supported by the U.S. Department of Energy, Office of Basic Energy Sciences, Division of Materials Sciences and Engineering and performed, in part, at the Center for Integrated Nanotechnologies, an Office of Science User Facility operated for the U.S. Department of Energy (DOE) Office of Science. Sandia National Laboratories is a multimission laboratory managed and operated by National Technology and Engineering Solutions of Sandia, LLC., a wholly owned subsidiary of Honeywell International, Inc., for the U.S. Department of Energy's National Nuclear Security Administration under contract DE-NA-0003525. This article describes objective technical results and analysis. The views expressed in the article do not necessarily represent the views of the U.S. DOE or the United States Government.

■ REFERENCES

- (1) Keller, U. Recent developments in compact ultrafast lasers. *Nature* **2003**, *424*, 831.
- (2) Quarterman, A. H.; Wilcox, K. G.; Apostolopoulos, V.; Mihoubi, Z.; Elsmere, S. P.; Farrer, I.; Ritchie, D. A.; Tropper, A. A passively mode-locked external-cavity semiconductor laser emitting 60-fs pulses. *Nat. Photonics* **2009**, *3*, 729.

- (3) Keller, U.; Weingarten, K.J.; Kartner, F.X.; Kopf, D.; Braun, B.; Jung, I.D.; Fluck, R.; Honninger, C.; Matuschek, N.; Aus der Au, J. Semiconductor saturable absorber mirrors (SESAM's) for femto-second to nanosecond pulse generation in solid-state lasers. *IEEE J. Sel. Top. Quantum Electron.* **1996**, *2*, 435–453.

- (4) Havstad, S. A.; Fischer, B.; Willner, A. E.; Wickham, M. G. Loop-mirror filters based on saturable-gain or-absorber gratings. *Opt. Lett.* **1999**, *24*, 1466–1468.

- (5) Wang, J.-C.; Sun, C.-K.; Wang, J.-K. Nonlinear pulse-shaping phenomena of semiconductor saturable absorber mirror. *Appl. Phys. Lett.* **2006**, *89*, 231106.

- (6) Vignaud, D.; Lampin, J. F.; Mollot, F. Two-photon absorption in InP substrates in the 1.55 μm range. *Appl. Phys. Lett.* **2004**, *85*, 239–241.

- (7) Spühler, G. J.; Weingarten, K. J.; Grange, R.; Krainer, L.; Haiml, M.; Liverini, V.; Golling, M.; Schön, S.; Keller, U. Semiconductor saturable absorber mirror structures with low saturation fluence. *Appl. Phys. B: Lasers Opt.* **2005**, *81*, 27–32.

- (8) Li, G.; Yao, B. Q.; Meng, P. B.; Wang, W.; Ju, Y. L.; Wang, Y. Z. InGaAs/GaAs saturable absorber for diode-pumped passively Q-switched mode-locking of Tm,Ho:YVO₄ laser. *Laser Phys. Lett.* **2011**, *8*, 42–45.

- (9) Schmidt, A.; Rivier, S.; Steinmeyer, G.; Yim, J. H.; Cho, W. B.; Lee, S.; Rotermund, F.; Pujol, M. C.; Mateos, X.; Aguiló, M.; Díaz, F.; Petrov, V.; Griebner, U. Passive mode locking of Yb:KLuW using a single-walled carbon nanotube saturable absorber. *Opt. Lett.* **2008**, *33*, 729–731.

- (10) Martinez, A.; Yamashita, S. Multi-gigahertz repetition rate passively modelocked fiber lasers using carbon nanotubes. *Opt. Express* **2011**, *19*, 6155–6163.

- (11) Martinez, A.; Sun, Z. Nanotube and graphene saturable absorbers for fibre lasers. *Nat. Photonics* **2013**, *7*, 842.

- (12) Bao, Q.; Zhang, H.; Wang, Y.; Ni, Z.; Yan, Y.; Shen, Z. X.; Loh, K. P.; Tang, D. Y. Atomic-layer graphene as a saturable absorber for ultrafast pulsed lasers. *Adv. Funct. Mater.* **2009**, *19*, 3077–3083.

- (13) Bonaccorso, F.; Sun, Z.; Hasan, T.; Ferrari, A. Graphene photonics and optoelectronics. *Nat. Photonics* **2010**, *4*, 611.

- (14) Bao, Q.; Zhang, H.; Ni, Z.; Wang, Y.; Polavarapu, L.; Shen, Z.; Xu, Q.-H.; Tang, D.; Loh, K. P. Monolayer graphene as a saturable absorber in a mode-locked laser. *Nano Res.* **2011**, *4*, 297–307.

- (15) Saraceno, C. J.; Schriber, C.; Mangold, M.; Hoffmann, M.; Heckl, O. H.; Baer, C. R.; Golling, M.; Südmeyer, T.; Keller, U. SESAMs for high-power oscillators: design guidelines and damage thresholds. *IEEE J. Sel. Top. Quantum Electron.* **2012**, *18*, 29–41.

- (16) Diebold, A.; Zengerle, T.; Alfieri, C. G. E.; Schriber, C.; Emaury, F.; Mangold, M.; Hoffmann, M.; Saraceno, C. J.; Golling, M.; Follman, D.; Cole, G. D.; Aspelmeyer, M.; Südmeyer, T.; Keller, U. Optimized SESAMs for kilowatt-level ultrafast lasers. *Opt. Express* **2016**, *24*, 10512–10526.

- (17) Brovelli, L. R.; Keller, U.; Chiu, T. H. Design and operation of antiresonant Fabry–Perot saturable semiconductor absorbers for mode-locked solid-state lasers. *J. Opt. Soc. Am. B* **1995**, *12*, 311–322.

- (18) Guerreiro, P. T.; Ten, S.; Borrelli, N. F.; Butty, J.; Jabbour, G. E.; Peyghambarian, N. PbS quantum-dot doped glasses as saturable absorbers for mode locking of a Cr:forsterite laser. *Appl. Phys. Lett.* **1997**, *71*, 1595–1597.

- (19) Malyarevich, A. M.; Savitski, V. G.; Prokoshin, P. V.; Posnov, N. N.; Yumashev, K. V.; Raaben, E.; Zhilin, A. A. Glass doped with PbS quantum dots as a saturable absorber for 1- μm neodymium lasers. *J. Opt. Soc. Am. B* **2002**, *19*, 28–32.

- (20) Camacho-Morales, R.; et al. Nonlinear generation of vector beams from AlGaAs nanoantennas. *Nano Lett.* **2016**, *16*, 7191–7197.

- (21) Kruk, S. S.; Camacho-Morales, R.; Xu, L.; Rahmani, M.; Smirnova, D. A.; Wang, L.; Tan, H. H.; Jagadish, C.; Neshev, D. N.; Kivshar, Y. S. Nonlinear optical magnetism revealed by second-harmonic generation in nanoantennas. *Nano Lett.* **2017**, *17*, 3914–3918.

- (22) Meinzer, N.; Barnes, W. L.; Hooper, I. R. Plasmonic meta-atoms and metasurfaces. *Nat. Photonics* **2014**, *8*, 889–898.

- (23) Smirnova, D.; Kivshar, Y. S. Multipolar nonlinear nanophotonics. *Optica* **2016**, *3*, 1241–1255.
- (24) Li, G.; Zhang, S.; Zentgraf, T. Nonlinear photonic metasurfaces. *Nat. Rev. Mater.* **2017**, DOI: 10.1038/natrev-mats.2017.10.
- (25) Krasnok, A.; Tymchenko, M.; Alù, A. Nonlinear metasurfaces: A paradigm shift in nonlinear optics. *Mater. Today* **2018**, *21*, 8–21.
- (26) Klein, M. W.; Enkrich, C.; Wegener, M.; Linden, S. Second-harmonic generation from magnetic metamaterials. *Science* **2006**, *313*, 502–504.
- (27) Carletti, L.; Locatelli, A.; Stepanenko, O.; Leo, G.; De Angelis, C. Enhanced second-harmonic generation from magnetic resonance in AlGaAs nanoantennas. *Opt. Express* **2015**, *23*, 26544–26550.
- (28) Gili, V. F.; Carletti, L.; Locatelli, A.; Rocco, D.; Finazzi, M.; Ghirardini, L.; Favero, I.; Gomez, C.; Lemaitre, A.; Celebrano, M.; De Angelis, C.; Leo, G.; et al. Monolithic AlGaAs second-harmonic nanoantennas. *Opt. Express* **2016**, *24*, 15965–15971.
- (29) Vabishchevich, P. P.; Liu, S.; Sinclair, M. B.; Keeler, G. A.; Peake, G. M.; Brener, I. Enhanced Second-Harmonic Generation Using Broken Symmetry III–V Semiconductor Fano Metasurfaces. *ACS Photonics* **2018**, *5*, 1685.
- (30) Smirnova, D.; Smirnov, A. I.; Kivshar, Y. S. Multipolar second-harmonic generation by Mie-resonant dielectric nanoparticles. *Phys. Rev. A: At., Mol., Opt. Phys.* **2018**, *97*, 013807.
- (31) Shcherbakov, M. R.; Neshev, D. N.; Hopkins, B.; Shorokhov, A. S.; Staude, I.; Melik-Gaykazyan, E. V.; Decker, M.; Ezhov, A. A.; Miroshnichenko, A. E.; Brener, I.; Fedyanin, A. A.; Kivshar, Y. S. Enhanced third-harmonic generation in silicon nanoparticles driven by magnetic response. *Nano Lett.* **2014**, *14*, 6488–6492.
- (32) Grinblat, G.; Li, Y.; Nielsen, M. P.; Oulton, R. F.; Maier, S. A. Enhanced third harmonic generation in single germanium nanodisks excited at the anapole mode. *Nano Lett.* **2016**, *16*, 4635–4640.
- (33) Shorokhov, A. S.; Melik-Gaykazyan, E. V.; Smirnova, D. A.; Hopkins, B.; Chong, K. E.; Choi, D.-Y.; Shcherbakov, M. R.; Miroshnichenko, A. E.; Neshev, D. N.; Fedyanin, A. A.; Kivshar, Y. S. Multifold enhancement of third-harmonic generation in dielectric nanoparticles driven by magnetic Fano resonances. *Nano Lett.* **2016**, *16*, 4857–4861.
- (34) Li, Z.; Palacios, E.; Butun, S.; Aydin, K. Visible-frequency metasurfaces for broadband anomalous reflection and high-efficiency spectrum splitting. *Nano Lett.* **2015**, *15*, 1615–1621.
- (35) Wurtz, G. A.; Pollard, R.; Hendren, W.; Wiederrecht, G. P.; Gosztola, D. J.; Podolskiy, V. A.; Zayats, A. V. Designed ultrafast optical nonlinearity in a plasmonic nanorod metamaterial enhanced by nonlocality. *Nat. Nanotechnol.* **2011**, *6*, 107–111.
- (36) Shcherbakov, M. R.; Vabishchevich, P. P.; Shorokhov, A. S.; Chong, K. E.; Choi, D.-Y.; Staude, I.; Miroshnichenko, A. E.; Neshev, D. N.; Fedyanin, A. A.; Kivshar, Y. S. Ultrafast All-Optical Switching with Magnetic Resonances in Nonlinear Dielectric Nanostructures. *Nano Lett.* **2015**, *15*, 6985–6990.
- (37) Krasnok, A.; Li, S.; Lepeshov, S.; Savelev, R.; Baranov, D. G.; Alù, A. All-Optical Switching and Unidirectional Plasmon Launching with Nonlinear Dielectric Nanoantennas. *Phys. Rev. Appl.* **2018**, *9*, 014015.
- (38) Kuznetsov, A. I.; Miroshnichenko, A. E.; Brongersma, M. L.; Kivshar, Y. S.; Luk'yanchuk, B. Optically resonant dielectric nanostructures. *Science* **2016**, *354*, aag2472.
- (39) Decker, M.; Staude, I. Resonant dielectric nanostructures: a low-loss platform for functional nanophotonics. *J. Opt.* **2016**, *18*, 103001.
- (40) Zhu, A. Y.; Kuznetsov, A. I.; Luk'yanchuk, B.; Engheta, N.; Genevet, P. Traditional and emerging materials for optical metasurfaces. *Nanophotonics* **2017**, *6*, 452–471.
- (41) Yang, Y.; Kravchenko, I. I.; Briggs, D. P.; Valentine, J. All-dielectric metasurface analogue of electromagnetically induced transparency. *Nat. Commun.* **2014**, *5*, 5753.
- (42) Moitra, P.; Slovick, B. A.; Li, W.; Kravchenko, I. I.; Briggs, D. P.; Krishnamurthy, S.; Valentine, J. Large-Scale All-Dielectric Metamaterial Perfect Reflectors. *ACS Photonics* **2015**, *2*, 692–698.
- (43) Liu, S.; Keeler, G. A.; Reno, J. L.; Sinclair, M. B.; Brener, I. III–V Semiconductor Nanoresonators—A New Strategy for Passive, Active, and Nonlinear All-Dielectric Metamaterials. *Adv. Opt. Mater.* **2016**, *4*, 1457–1462.
- (44) Liu, S.; Sinclair, M. B.; Saravi, S.; Keeler, G. A.; Yang, Y.; Reno, J.; Peake, G. M.; Setzpfandt, F.; Staude, I.; Pertsch, T.; Brener, I. Resonantly Enhanced Second-Harmonic Generation Using III–V Semiconductor All-Dielectric Metasurfaces. *Nano Lett.* **2016**, *16*, 5426–5432.
- (45) Löchner, F. J. F.; Fedotova, A. N.; Liu, S.; Keeler, G. A.; Peake, G. M.; Saravi, S.; Shcherbakov, M. R.; Burger, S.; Fedyanin, A. A.; Brener, I.; Pertsch, T.; Setzpfandt, F.; Staude, I. Polarization-Dependent Second Harmonic Diffraction from Resonant GaAs Metasurfaces. *ACS Photonics* **2018**, *5*, 1786.
- (46) Shcherbakov, M. R.; Liu, S.; Zubyuk, V. V.; Vaskin, A.; Vabishchevich, P. P.; Keeler, G.; Pertsch, T.; Dolgova, T. V.; Staude, I.; Brener, I.; Fedyanin, A. A. Ultrafast all-optical tuning of direct-gap semiconductor metasurfaces. *Nat. Commun.* **2017**, DOI: 10.1038/s41467-017-00019-3.
- (47) Staude, I.; Miroshnichenko, A. E.; Decker, M.; Fofang, N. T.; Liu, S.; Gonzales, E.; Dominguez, J.; Luk, T. S.; Neshev, D. N.; Brener, I.; Kivshar, Y. Tailoring directional scattering through magnetic and electric resonances in subwavelength silicon nanodisks. *ACS Nano* **2013**, *7*, 7824–7832.
- (48) Melik-Gaykazyan, E. V.; Shcherbakov, M. R.; Shorokhov, A. S.; Staude, I.; Brener, I.; Neshev, D. N.; Kivshar, Y. S.; Fedyanin, A. A. Third-harmonic generation from Mie-type resonances of isolated all-dielectric nanoparticles. *Philos. Trans. R. Soc., A* **2017**, *375*, 20160281.
- (49) Arslan, D.; Chong, K.; Miroshnichenko, A.; Choi, D.; Neshev, D.; Pertsch, T.; Kivshar, Y.; Staude, I. Angle-selective all-dielectric Huygens' metasurfaces. *J. Phys. D: Appl. Phys.* **2017**, *50*, 434002.
- (50) Sell, D. D.; Casey, H. C.; Wecht, K. W. Concentration dependence of the refractive index for n- and p-type GaAs between 1.2 and 1.8 eV. *J. Appl. Phys.* **1974**, *45*, 2650–2657.
- (51) Blakemore, J. S. Semiconducting and other major properties of gallium arsenide. *J. Appl. Phys.* **1982**, *53*, R123–R181.
- (52) Dancus, I.; Vlad, V.; Petris, A.; Rujoiu, T. B.; Rau, I.; Kajzar, F.; Meghea, A.; Tane, A. Z-Scan and I-Scan methods for characterization of DNA optical nonlinearities. *Rom. Rep. Phys.* **2013**, *65*, 966.
- (53) Taheri, B.; Liu, H.; Jassemnejad, B.; Appling, D.; Powell, R. C.; Song, J. Intensity scan and two photon absorption and nonlinear refraction of C60 in toluene. *Appl. Phys. Lett.* **1996**, *68*, 1317–1319.
- (54) Bennett, B. R.; Soref, R. A.; Del Alamo, J. A. Carrier-induced change in refractive index of InP, GaAs and InGaAsP. *IEEE J. Quantum Electron.* **1990**, *26*, 113–122.
- (55) Palik, E. D. *Handbook of Optical Constants of Solids*; Academic Press, 1985.
- (56) Wurtz, G. A.; Pollard, R.; Hendren, W.; Wiederrecht, G.; Gosztola, D.; Podolskiy, V.; Zayats, A. V. Designed ultrafast optical nonlinearity in a plasmonic nanorod metamaterial enhanced by nonlocality. *Nat. Nanotechnol.* **2011**, *6*, 107.
- (57) Ren, M.; Jia, B.; Ou, J.-Y.; Plum, E.; Zhang, J.; MacDonald, K. F.; Nikolaenko, A. E.; Xu, J.; Gu, M.; Zheludev, N. I. Nanostructured plasmonic medium for terahertz bandwidth all-optical switching. *Adv. Mater.* **2011**, *23*, 5540–5544.
- (58) Cho, D. J.; Wu, W.; Ponizovskaya, E.; Chaturvedi, P.; Bratkovsky, A. M.; Wang, S.-Y.; Zhang, X.; Wang, F.; Shen, Y. R. Ultrafast modulation of optical metamaterials. *Opt. Express* **2009**, *17*, 17652–17657.
- (59) Tuz, V. R.; Khardikov, V. V.; Kupriyanov, A. S.; Domina, K. L.; Xu, S.; Wang, H.; Sun, H.-B. High-quality trapped modes in all-dielectric metamaterials. *Opt. Express* **2018**, *26*, 2905–2916.
- (60) Lim, W. X.; Singh, R. Universal behaviour of high-Q Fano resonances in metamaterials: terahertz to near-infrared regime. *Nano Convergence* **2018**, *5*, 5.
- (61) Tittel, A.; Leitis, A.; Liu, M.; Yesilkoy, F.; Choi, D.-Y.; Neshev, D. N.; Kivshar, Y. S.; Altug, H. Imaging-based molecular barcoding with pixelated dielectric metasurfaces. *Science* **2018**, *360*, 1105–1109.

(62) Koshelev, K.; Lepeshov, S.; Liu, M.; Bogdanov, A.; Kivshar, Y. Asymmetric metasurfaces with high-Q resonances governed by bound states in the continuum. *Phys. Rev. Lett.* **2018**, *121*, 193903.